Probing Flow Activity in Polyamide Layer of Reverse Osmosis Membrane with Nanoparticle Tracers

Yuqiong Li,[a] Michał M. Kłosowski,[b] Catriona M. McGilvery,[b] Alexandra E. Porter,[b] Andrew G. Livingston,[a] and João T. Cabral[a]*

[a]*Department of Chemical Engineering,* [b]*Department of Materials,*
Imperial College London, London SW7 2AZ
**Email: j.cabral@imperial.ac.uk, Tel: +44 207 594 5571*

Keywords: *thin film composite, reverse osmosis, nanoparticles, and characterization*

Abstract

We investigate the flow activity of the nanostructured polyamide layer in reverse osmosis (RO) membrane, using gold nanoparticle (NP) tracers of 1-40 nm diameter. Following a detailed structural examination of a commercial SW30RH membrane selected for this study, NP solutions were infiltrated from either the polyamide front or the polysulfone support side. The permeate was then analyzed spectroscopically while the entrapment of NPs within the membrane was mapped by high resolution electron microscopy. Results show that back-filtered NPs exhibited a fractionated distribution according to size: 1 nm nanoparticles permeate across the polyamide-polysulfone interface reaching the interior of the polyamide corrugations, while the larger ones (>10 nm) are retained within the polysulfone and gradually arrested at approximately 100 nm below the polyamide-polysulfone interface. Intermediate-sized 5 nm nanoparticles reached the undulating folds just below the polyamide layer. Permeation pathways across polyamide layer appear to exclude all tracers above 1 nm, which become selectively distributed across the polyamide layer: positively charged NPs label the outer surface of the polyamide film (expected to be carboxylate-rich), while negatively charged particles are uniformly distributed within the layer. Diafiltration measurements quantify the transient kinetics of NP retention and permeation. Overall, our results establish the flow activity of the polyamide nodular surface and provide estimates for the dimensions of permeation pathways.

1. Introduction

Reverse Osmosis (RO) is widely recognized for its low energy usage and reduced environmental footprint, and is thus employed in sea water desalination and industrial water purification.[1,2] Within the oil and gas industry, low-salinity water obtained by RO is extensively used in offshore drilling to increase oil recovery from sandstone reservoirs.[3,4] A typical RO membrane is a composite structure comprising a layer of fully cross-linked aromatic polyamide (PA) nanofilm, a porous polysulfone (PSf) support layer and a polyester (PET) fabric backing layer. The PA layer has an overall

thickness of approximately 200-500 nm,[2] depending on spatial variations and membrane type, and the PSf layer is 50-100 μm thick. The PET layer provides the mechanical support for membrane handling and operation. The full RO membrane is referred to as a thin film composite (TFC) membrane because of the layered PA-PSf-PET structure.

The PA thin film is generally fabricated onto the phase-inverted PSf support layer by an interfacial polymerization reaction between m-phenylenediamine (MPD) and trimesoylchloride (TMC).[5,6,7]. This results in a highly heterogeneous, rough surface with many protruding, nodular features. It has recently been reported from cross-sectional transmission electron microscopy (TEM) and atomic force microscopy (AFM) [5,6] that the PA membrane layer comprises 'crumpled' films, whose individual thickness is approximately 10 nm. Crumpling results in the large roughness, heterogeneity, and surface contour, yielding the overall 200-500 nm PA thickness.[2] These contrast to nanofiltration (NF) membranes prepared from piperazine and TMC which generally yield smooth, flat surfaces.[8] RO membranes are therefore distinct in both morphology and salt rejection performance.

However, a clear link between active layer nanostructure, support layer, and water and salt transport remains, so far, elusive. Transport through thin film composite (TFC) membranes has been reported to depend on both the permeability and selectivity of the PA layer, and the pore morphology of the underlying PSf support.[9,10,11] However, the role of the surface crumpling, heterogeneity, and voids within the PA layer, as well as the nature of the PA/PSf interface, in terms of flow activity and nanoporosity are yet to be understood. Cross-sectional structures of many synthetic polymeric membranes have been recently reported.[12,13,14,15] Wong *et al*. provided evidence of the existence of voids in SW30HR and XLE membranes

using TEM, whose overall volume was estimated to be approximately 30%[12] Lin *et al.* applied a combination of TEM, quartz crystal microbalance (QCM) and spectroscopic ellipsometry to estimate the void fraction in a range of membranes from NF (NF90) to RO (SW30HR, XLE, ESPA3, SWC4+).[13] Recently, Pacheco *et al.* employed TEM tomography to resolve the 3D structure of the voids within the PA layer in ESPA3 and SWC3 membranes,[14] reconstructing the spatial distribution of void volumes down to a lengthscale of approximately 15 nm. A positive correlation between the presence of nanometer scale voids and surface undulations of the PA active layer, has been found to be consistent with a higher water permeance.[13,14]

A number of characterization techniques are routinely used to investigate the morphology, roughness and porosity of such RO membranes.[5,16,17,18] Given the amorphous structure of the polymers, direct imaging of permeation pathways by electron microscopy is challenging due to the low electron contrast in the membrane and the non-rigid and non-linear structure of the pathways.[16] Techniques such as (energy variable) positron annihilation lifetime spectroscopy (PALS),[19,20] and neutron or X-ray reflectometry [21,22,23] provide depth-averaged free-volume estimates (electron or scattering length) of density with angstrom to nanometer (Å-nm) resolution, but cannot resolve actual permeation pathways or free volume connectivity. Further, polymeric materials exhibit rich, dynamic processes[24] (from the atomic to segmental and cooperative reorganization) that are likely coupled with solute transport, but are inaccessible to these structural probes. Visualization at the nanoscale in the hydrated state has thus not been reported.

Nanoparticles (NPs) and stains can effectively aid visualization by enhancing contrast in membrane imaging, and enabling the study of particle-membrane interactions.[25] Rizwan *et al.* showed that NPs preferentially accumulate near the “peaks” and not the

"valleys" of the rough NF membrane surface.[25] A method for determining the skin thickness of ultrafiltration (UF) membranes was developed by Cuperus *et al.*[26] in which poly (2,6-dimethyl-1,4-phenylene oxide) (PPO) and PSf membranes were investigated using colloidal gold NPs of 6 nm and 50 nm average sizes. SEM was then used to image the cross-sectional areas of the membranes, and revealed a well-defined skin layer where even the smallest gold NPs failed to penetrate. Similarly, Stawikowska *et al.* used osmium dioxide NPs, adsorbed with polystyrene, and filtered into integrally skinned asymmetric organic solvent nanofiltration (OSN) membranes, which have larger pores than RO membranes and are not TFCs.[27, 28] However, significant questions remained relating to particle geometry, its polydispersity and interpretation of the contrast in relatively thick TEM sections.

In this paper, we extend these studies by considering the flow through a model, high salt rejection RO membrane SW30HR using NP tracers (gold 1-40 nm diameter, of positive and negative charge) with are infiltrated from either the front or back side of the membrane. We then track their spatial distribution, seeking to resolve transport active pathways through the PSf and PA layers under relevant operating conditions. This approach provides thus a proxy for *in operando* visualization, since the NP tracers are infiltrated during filtration, and resulting NP distribution is then mapped at the nanoscale by electron microscopy. Diafiltration measurements provide further insight into the transient behavior during NP infiltration, and elucidate the asymptotic distribution of NP within the membrane structure.

2. Experimental Section

2.1. RO Membrane and Nanoparticle Imaging Agents

The membrane selected for this work is the commercial, high rejection seawater flat sheet membrane, SW30-HR® (FilmTech™ FT-30 series), purchased from Sterlitech Co. Gold (Au) NPs of diameters 5, 10, 20, 40 nm (negatively charged) suspended in H_2O were purchased from BBI® Solutions, and 1 nm, both positively and negatively charged, from Undecagold® Nanoprobes. The 1nm NPs were received as a dry powder and were dissolved in deionized H_2O to form the solution. The size and distribution of the nanoparticles were characterized by Dynamic Light Scattering (DLS, Malvern Zetasizer Nano series) and by UV-Vis spectroscopy (Shimadzu), as shown in SI Figure S1 and Table S1.

2.2. Batch Filtration

Batch dead-end filtration experiments, using a stirred ultrafiltration cell (Millipore), were used to investigate transport of particles through the membrane and measure salt rejection, as illustrated in Figure 1a. A volume of 3 mL of NP solution (5×10^{12} particles/mL for the 5-40 nm particles and $3x10^{15}$ particles/ml for the 1 nm particles) was filtered through a membrane coupon of 25 mm diameter under a pressure of 3 bar at the front, and a pressure of 1 bar in the back. Filtration experiments were run at room temperature until completion. For each NP size, and filtration experiment (at least 3 repeats per NP size), a separate membrane coupon was employed. Nanoparticle rejection was measured when the initial feed volume had halved. The concentration of particles in the permeate and retentate were quantified by UV-vis spectroscopy. Uncertainties were computed from maximum deviation between measurements.

2.3. Diafiltration

Diafiltration was used to measure NP transport over a time period corresponding to

10 diavolumes, for the smallest NPs, 1 nm (+) and 1 nm (-) in back-filtration, illustrated in Figure 1b. The pH conditions were carefully maintained at neutral value for all NP filtration experiments to prevent aggregation.

Back-filtration was performed in a 10 mL constant volume stirred cell under 4 bar pressure supplied by a high pressure liquid chromatography (HPLC) pump. An initial feed of 50 nmol of NPs dispersed in 10 mL of DI H_2O was used, and fresh DI H_2O was injected to keep the liquid volume in the stirred cell constant. The mass of NPs collected in accumulated permeate and mass of NPs remaining in the retentate were sampled every diavolume (equivalent to 10 mL) for a consecutive 10 volumes, and quantified by UV-vis spectroscopy.

Front-filtration was performed in a 10 mL constant volume stirred cell under 30 bar pressure supplied by a HPLC pump. As a control, a teflon disk was tested in the diafiltration cell with 5 nm, 1 nm (+) and 1 nm (-) NP solutions to measure any loss of NP in the system due to non-specific adsorption to tubing or cell (SI Figure S2).

By tracking the mass balance of nanoparticles within the membrane, the permeate and the retentate, more accurate estimates of particle permeation through the membrane and the fraction retained within the membrane could be obtained.

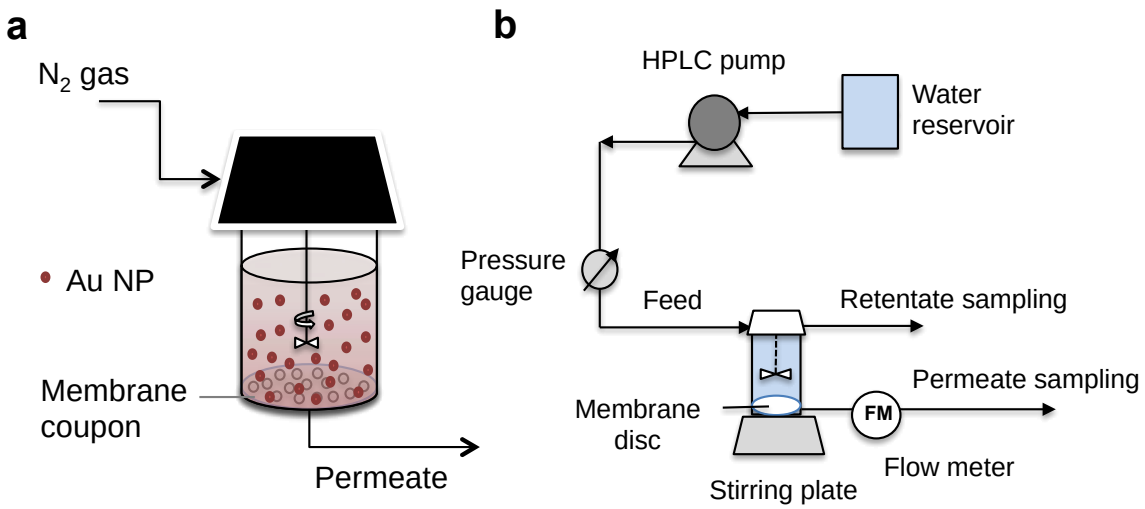

Figure 1: (a) Pressurized dead-end (batch) filtration cell set-up, and (b) diafiltration cell and schematic of NP solution concentration measurement.

2.4 Membrane Aging

To estimate the effect of ageing on permeance and rejection over time, membranes were aged in a cross-flow rig for 78 hr. The starting feed was sodium chloride (NaCl) solution at a concentration of 2 g/L and rejection data was obtained on a cross-flow rig operated at 20 bar for 78 h at room temperature. Salt concentration in the permeate and retentate were analyzed using a digital ion conductivity meter (HI-8633®).

2.5. Sample preparation for Imaging

Before and after filtration experiments, membranes were cross-sectioned for TEM imaging, using the following procedure: The polyester badking layer was peeled of. The samples were then dehydrated by three changes of 100% ethanol, allowing 30 minutes between each change. Samples were then immersed in 50% (2h), 67% (2h) and 100% (2h, twice) LR White resin (London Resin Company, purchased from Agar Scientific), where % corresponds to LR White diluted with ethanol by volume. Finally, samples were baked at 75°C overnight to allow the resin to set. LR white resin was

used as found to yield optimal contrast with these membranes. TEM sections (approximately 70 nm thick) were cut using an ultramicrotome (Leica) with a 35^{o} angle diamond knife, and then collected on 300-mesh holey-carbon copper grids and plain 300 mesh copper grids.

For STEM tomography experiments the polyamide films were isolated from their PSf support. This was done by attaching a small section of membrane, after the backing layer had been removed, to a TEM grid using a pair of tweezers. DMF or Chloroform were then dripped onto the membrane to dissolve and remove the PSf support. This left the isolated, PA layer on top of the copper grids for subsequent STEM imaging in plan-view.

Cross-sectional SEM samples were prepared by cryofracture. Strips of membrane samples were soaked in 100% ethanol for dehydration for over 2 h, and then immersed in liquid nitrogen for 5 min. Membranes were then fractured using a pair of tweezers, mounted onto 90^{o} angle SEM stubs, and coated with a 5 nm thick chromium layer to prevent charging. For plan view SEM imaging, a piece of membrane coupon was cut, mounted on an SEM stub and coated with chromium.

2.6. Characterization

Cross-sectional and surface topographic imaging was carried out using, scanning electron microscopy (SEM), TEM and scanning TEM (S)TEM imaging.

Secondary Electron imaging was carried out on a LEO Gemini 1525 field emission gun (FEG) SEM at 5 kV and a working distance of 6 mm, and a Zeiss Auriga FEG-SEM operated at 1.5 kV and a working distance of 5 mm. A JEOL 2000 FX equipped

with LaB_6 filament and operated at 80 kV was used for lower magnification bright-field TEM imaging.

Higher magnification TEM and STEM imaging was carried out on an image (C_s) corrected FEI Titan 80-300 (S)TEM microscope equipped with a Schottky FEG, operated at 300 kV. In STEM, images were acquired on an annular dark-field (ADF) detector with an inner and outer collection semi-angle of 26 and 145 mrad respectively and a convergence angle of 10 mrad. Under these conditions, bright contrast in the images is due to regions with higher atomic number and/or increased sample thickness. The contrast is inverted compared with bright-field TEM images. Generally, three disctinct membrane coupons, for each NP size, and typically 5-10 sample locations, were imaged to ensure reproducibility of results.

The Zeta potential of membrane surfaces was measured using Anton Paar SurPASS zeta potential apparatus following standard instrument operating protocols. In short, 600 mL of 1 mM KCl solution was used as the “fill” and “rinse” solution. A gap size of 100 μm was applied between the membrane surfaces facing each other. A pH range between 3 to 10 was tested.

UV-vis measurements of NP concentration, were carried out with a Shimadzu UV-vis spectrometer and quartz cuvette cells of 1 cm light path. Concentrations of NPs were calibrated using serial dilutions and calculated from Beer-Lambert Law. The λ_{max} of different NP sizes are shown in SI Figure S1c.

2.7 3-D Reconstruction of Tomographic Series

To understand the 3D structure of the membranes STEM tomography series of the plan view samples were acquired using the FEI TITAN 80/300. Images were taken at

tilt angles between +70 and -70 deg, at 2 deg increments. These 2D images were then combined, aligned and reconstructed using a simultaneous iterative reconstruction technique (SIRT) algorithm to create a 3D representation of the original sample.[29,30] The tilt series of images were reconstructed to yield 3D information about the sample. Inspect3D (FEI, Oregon, USA) was used to perform image reconstruction and Avizo3D (FEI, Oregon, USA) used to segment and visualise the structure. In Avizo the data was first filtered using a median filter, and then segmented by selecting a grey scale value where the voids and PA layer could be distinguished. This was a conservative estimate of contrast and further segmentation was done by hand. The smallest feature segmented was about 10nm in size. After this, an estimation of the free volume associated with structural voids was performed.

3. Results

3.1. EM Imaging of PA Layer Morphologies

The SEM images in Figure 2a show the thickness and morphology of the different layers within the RO membrane. In particular, the rough heterogeneous structure and complex morphology of the PA layer is clearly visible over several μm in Figure 2b. The TEM images in Figure 2c enable closer inspection of these features, identifying a variety of morphological features present in PA layer and two distinct regions in the PA layer – a more open structure towards the front surface and what initially appears to be a closed structure with discrete voids towards the PSf/PA interface. The degree of interconnectedness between these features is not, however, clear from these 2D images. It has been suggested[6,31] that the 'nodules' on the top surface may be formed from a tightly folded 10 nm PA membrane giving rise to a

'crumpled' surface. The roughness of the front and rear surfaces has been characterized by AFM and SEM (SI Figure S3) and the maximum peak to valley height measured to be 500 nm and 110 nm, respectively.

By reconstructing the volume of the membrane obtained from the TEM tomography series, larger voids (>50 nm) and interconnected regions were examined and visualised (SI Figure S4 and S5). In TEM cross sections these regions appear discrete; however, it was found that many of them are in fact interconnected and open to the outer surface and have been investigated in detail.[31] It was also possible to reconstruct discrete voids, of 5-50 nm in diameter, in the basal region of the PA layer from STEM tomography (SI Figure S5). Their morphology was observed and void volume fraction calculated to be approximately 27%, which agrees well with other reports. [12,13,14]

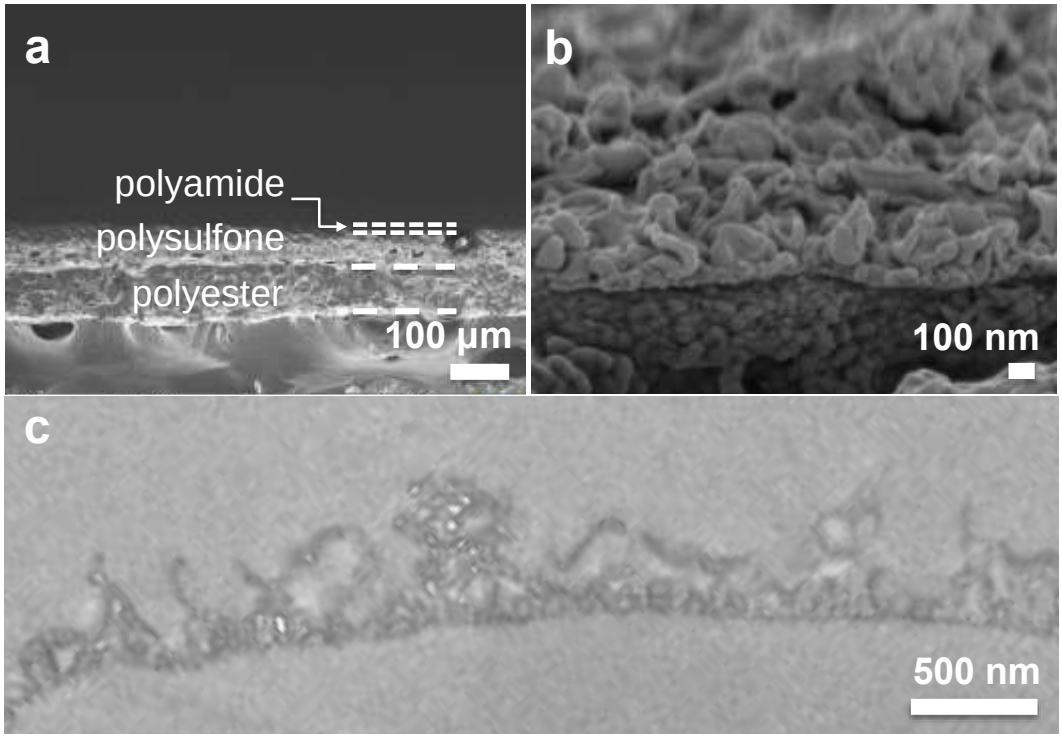

Figure 2: (a) SEM cross-sectional image of RO TFC exhibiting PA, PSf and PET three-layer structure; (b) Higher magnification SEM image of a cryofractured membrane sample; (c) Bright field TEM cross-sectional images of the membrane.

3.2. Batch Front-filtration of Au NPs

To investigate the connectivity of the void regions on the top surface, 5 nm NPs were front filtered through the membrane using a dead-end filtration cell, as detailed in Section 2.2. In Figure 3, the top surface of the PA layer is found to be covered with Au NPs, which agglomerate predominantly in the 'valley-like' regions of the membrane surface. It is observed that some nanoparticles reach apparent 'void'-like regions in the upper section of the PA membrane confirming that these have an open connection to the outer surface. In fact, nanoparticles reach to within 30 nm of the PA-PSf interface in some regions, showing that at least some of the holes in the basal region of the membrane are not discrete. Much of the basal region has not been accessed by the front-filtered 5 nm NPs. This may be due to a number of reasons: the dynamics of the filtration process may not have allowed all surface to be reached within the given time; the channels between different regions may be smaller than 5 nm and thus not accessible by these particles; or the regions may in fact be discrete, as tomography appears to indicate within the limitations of the technique.

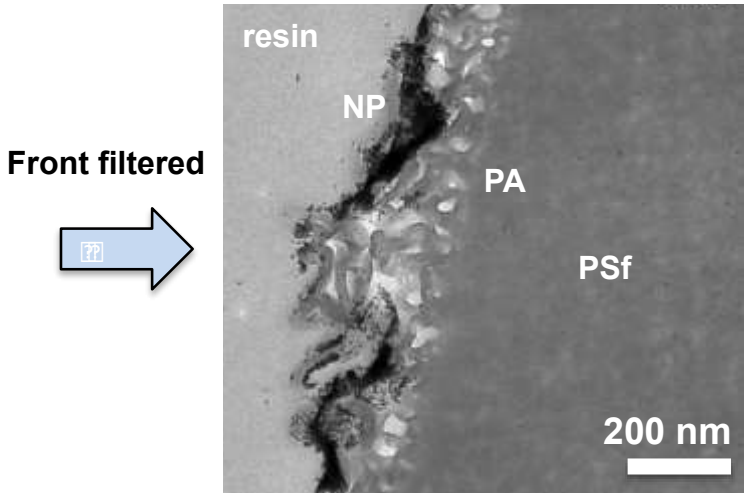

Figure 3: Bright field TEM cross-sectional images of RO membranes with 5 nm Au NPs front filtered onto membrane active surface.

3.3. Batch Back-filtration of Au NPs

The PA membranes following back filtration of 40, 20, 10, 5 and 1 nm Au NP solutions were examined, as described in section 2.2. TEM results are shown in Figures 4 and 5. We find NPs of 10, 20 and 40 nm NPs are completely retained within the PSf layer while a small fraction of 5 nm NPs appears to reach the PA-PSf interface. The distance to the PA-PSf interface was measured from the TEM images for about 100 NPs of each size (5 nm, 10 nm, 20 nm and 40 nm) (Figure 4). It is found that there is a 'clearance zone' away from the PA-PSf interface of approximately 200 nm that the larger 20-40 nm NPs cannot access. Such NP are able to penetrate the larger voids in the PSf but not the more densly packed polymer close to the PA-PSf interface. For the 10 nm NPs, this 'clearance' region is approximately 100 nm wide. Some of the 5 nm NPs can be found in the undulating folds just beneath the PA rear surface, however the majority of the NPs are retained within PSf. Figure 4e shows the size distribution graphically. Such size distributions provide an estimate of the dimensions of the transport pathways within PSf even though direct visualisation of sub-nm pathways is not feasible under these conditions. STEM images in Figure 5 show that back filtered Au NPs of 1 nm (the bright particles) of both (+) and (-) charge are clearly able to traverse the PA-PSf interface, reaching the PA film active layer.

A summary of the permeability of NPs of different sizes through pristine membranes, and also of salt permeation in aged membranes, is presented in Table 1. For the NP experiments it was found that all membranes exhibited 100% rejection, except for the case of the smallest (1 nm) particles where the rejection was between 97 and 99%.

Membranes exhibited significant physical ageing over time, exhibiting a gradual increase in salt rejection (NaCl), which we interpret as due to increased compaction of the membrane. Aged membranes show a salt rejection of around 80% at time zero to 98% over the course of 78 hours, which is also expected to restrict solute access. This is presumed to be due to a reduction in free volume and pathway connectivity.

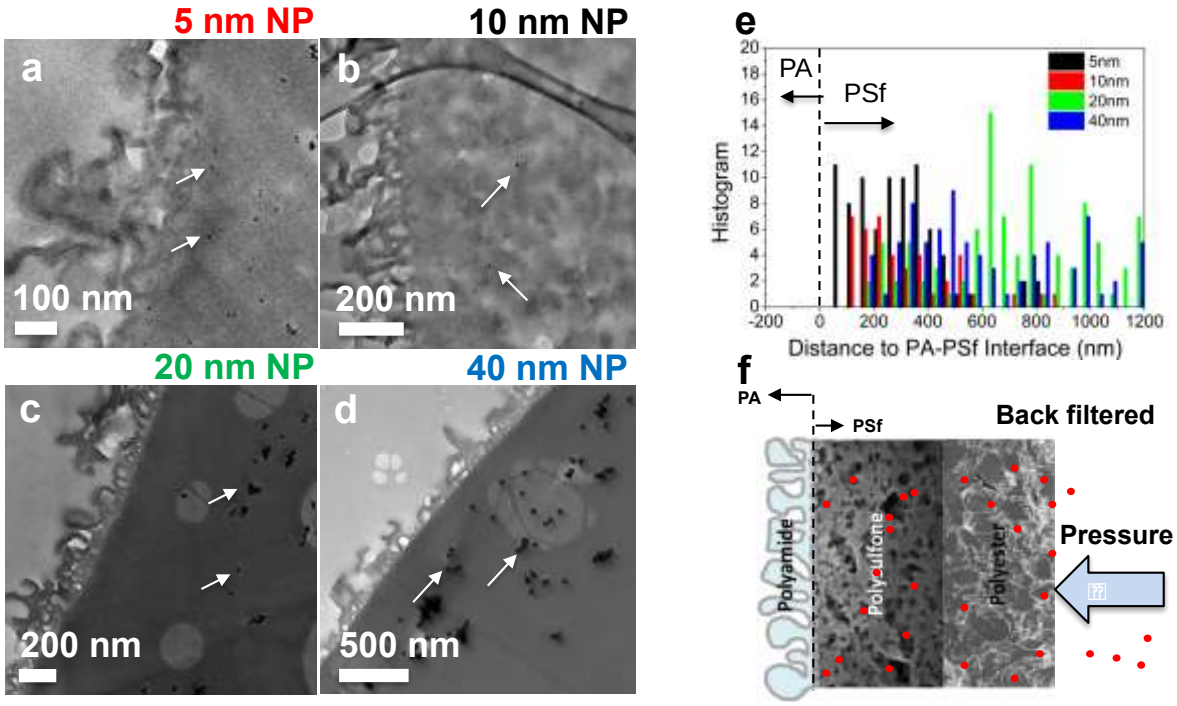

Figure 4: Bright field TEM cross-sectional images of TFC with (a) 5 nm, (b) 10 nm, (c) 20 nm, and (d) 40 nm gold (negatively charged) NPs back-filtered into the membrane. (e) Histogram showing the distances accessible to the NPs of different sizes with respect to the PA-PSf interface. (f) Schematic drawing showing the back filtration of NPs into the TFC.

Table 1: Rejection of NPs of different sizes and salt on unaged membranes.

Nanoparticles				Salt			
NP size (nm)	**Charge**	**Rejection back filtration (%)**	**Rejection front filtration (%)**	**NaCl (2g/L)**	**Time (hour)**	**Rejection front filtration (%)**	**Permeance (LMHBar)**
1 (+)	+	97 ± 5	99 ± 5		0	86	0.537
1 (-)	-	97 ± 5	99 ± 5		8	96	0.559
5	-	100	100		20	96	0.498
10	-	100	100		30	97	0.481
20	-	100	100		54	98	0.476
40	-	100	100		78	98	0.479

In order to controllably investigate the effects of solute charge, we employ Au NPs of approximately 1 nm with different surface charges: $7NH_3^+$ groups per Au particle for positive (+) NP and 27 COO^- groups per Au particle for negative (-) NP. Figure 6 shows zeta-potential measurements of the different size NPs at neutral pH and SW30HR membrane surface at various pH conditions. Under the experimental conditions considered (pH 6.8 for DI water), the 1 nm (+) NP has an expected surface charge of +36.67 mV, and the 1 nm (-) NP has a surface charge of -11.24mV. The surface of SW30HR remains negative for a pH range between 3 and 10. Back-filtration measurements suggest that the NP charge affects their distribution within the PA film, despite some sample-to-sample variability. From the images in Figure 5a-b, 1 nm (+) NPs appear to preferentially aggregate at the surface of the PA film (Figures 5a, and 9a, b at lower magnification) though are also present throughout the whole PA layer, while 1 nm (-) NPs exhibit a more uniform distribution, primarily at the PSf-PA interface with only a few passing into the bulk of the PA layer (Figure 5b, and SI Figures S6). The corresponding NP position distribution histogram is shown in Figure 5c. Here, instead of taking the PA/PSf interface as the reference, the PA-air interface is used, i.e. the distance normal to the (nearest) PA nanofilm surface. NP distances were thus estimated individually from the shortest distance

normal to the interface, and several NPs were analyzed for statistical significance.These results suggest that the 1 nm (+) NPs exhibit a bimodal distribution with respect to the PA surface. The first group of peaks at about 1 nm are due to NPs sitting close to the air/PA interface; the second band of peaks with a maximum at around 45 nm is due to NPs at the PA/PSf interface. This is in contrast to the monotonic profile of 1 nm (-) NPs where the particles are homogeneously dispersed across the PA layer. These results from imaging and absorption data suggest that there is a charge distribution across the PA layer influenced by specific functional groups in and on the surface of the membrane. A charge distribution due to functional groups has been previously reported in the literature.[2, 32, 33]

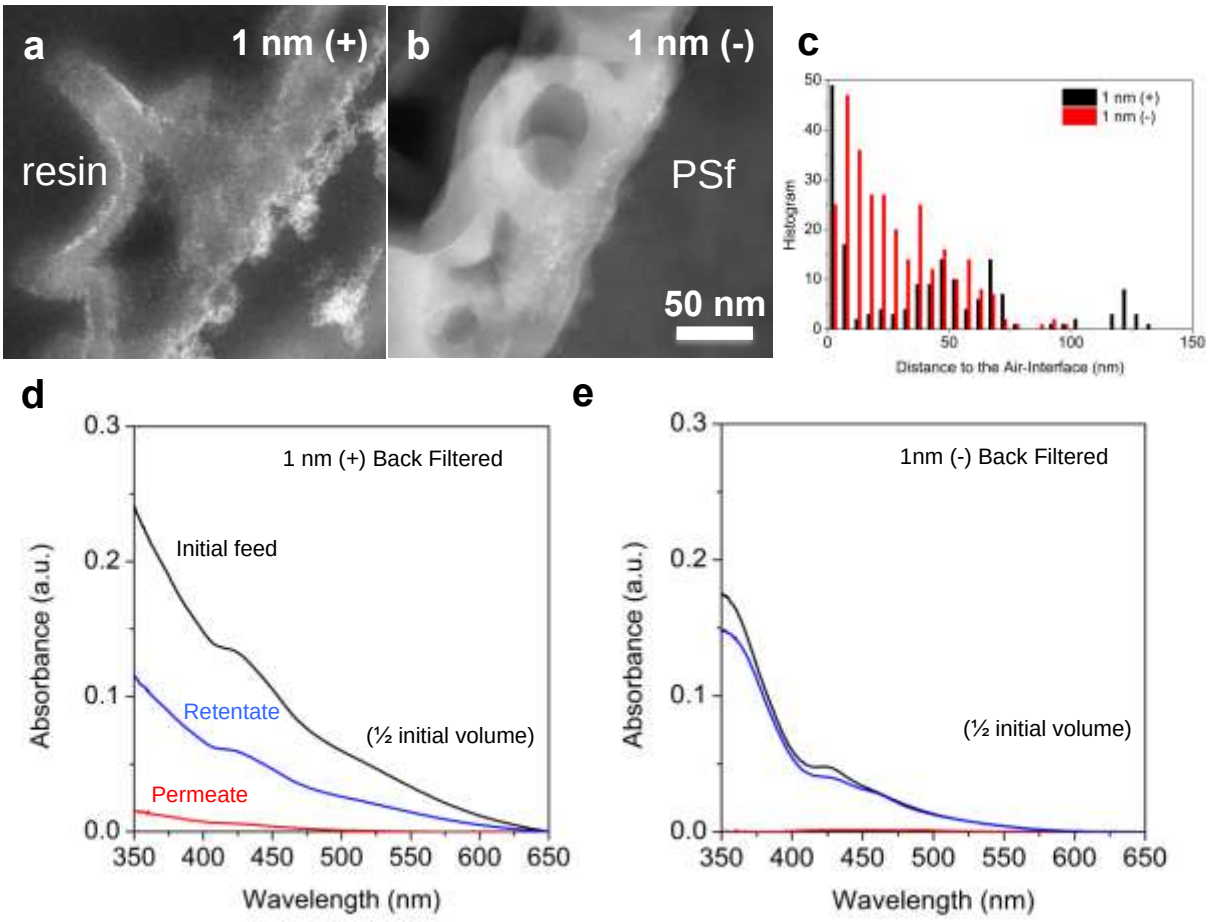

Figure 5: (a) and (b) ADF-STEM images of backfiltered 1 nm NP of (+) and (-) surface charges, respectively; (c) corresponding histogram of NP position with respect to the air-interface, whose Y-axis represents number frequency of NPs; (d)-

(e) Rejection measurements of the 1 nm (+) and (-) NPs which are summarized in Table 1. Concentrations of NPs are measured by UV-vis absorbance.

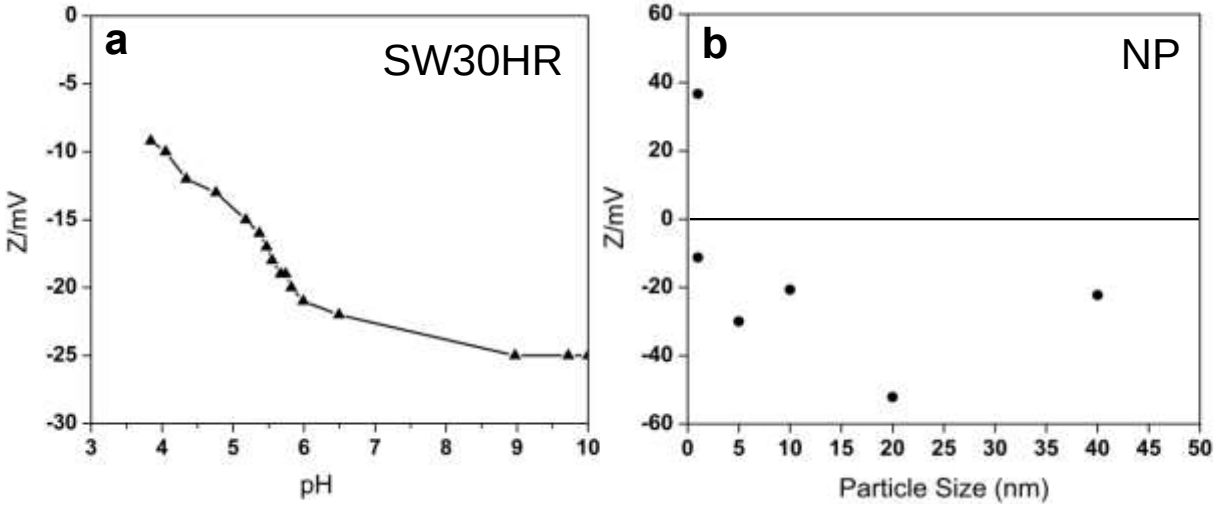

Figure 6: Zeta-potential measurement data of (a) SW30HR membrane surface from pH 3-10, and (b) Au NPs of various sizes, at neutral pH 6.8.

3.4. Diafiltration of 1 nm NPs in Back Filtration Mode

From the diafiltration experiments, both 1 nm (+) and 1 nm (-) NPs are observed to accumulate within the membrane for subsequent diavolume collections (Figure 7). At the end of 10 diavolumes, about 75% of 1 nm (+) NPs are retained inside the membrane, while an accumulated amount of NPs (25% of the initial feed mass) are measured to have permeated out of the membrane; similarly for 1 nm (-) NPs, about 67% is lost inside the membrane and approximately 32% of the initial feed mass is measured to permeate out of the membrane; the remaining 1% of NPs is in the retentate. In the control experiment with a teflon disk, maximum non-spectific adsorption in the system is observed with 1 nm (+) NP, at around 10% initial feed mass, while 1 nm (-) NP and 5 nm NP both show minimum adsorption in the system at less than 5% mass loss (SI Figure S2). The observation of 1 nm NPs permeating through the membrane in diafiltration is confirmed by TEM imaging, where the NPs are found to be present within the crumpled nodules on the top surface of the PA film

(Figure 8). Despite the large number of NPs injected and considerable rejection of ~70%, a comparatively small fraction is visible in Figure 8 (normalized by surface area). We interpret this observation as due to retention taking place throughout the entirety of the membrane depth, including the PSf layer. This observation strongly suggests that such nodules are flow active to both water and solutes such as 1 nm NPs (Figure 7, 8).

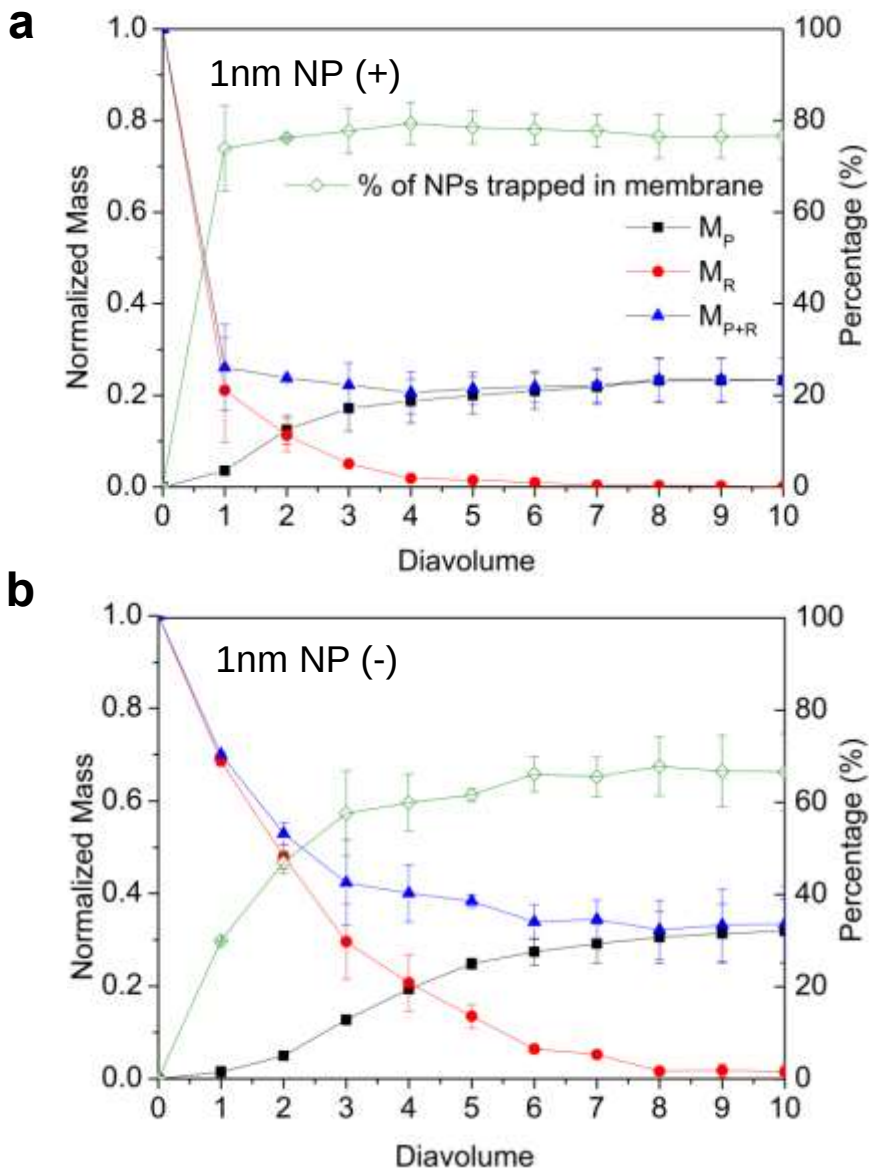

Figure 7: Change in mass of collected permeate (black ■), retentate (red ●), combined mass of permeate and retentate (blue ▲) and percentage loss of particle mass inside the membrane (green ◊) over the course of 10 diafiltration runs for (a) 1 nm (+) NP and (b) 1 nm (-) NP.

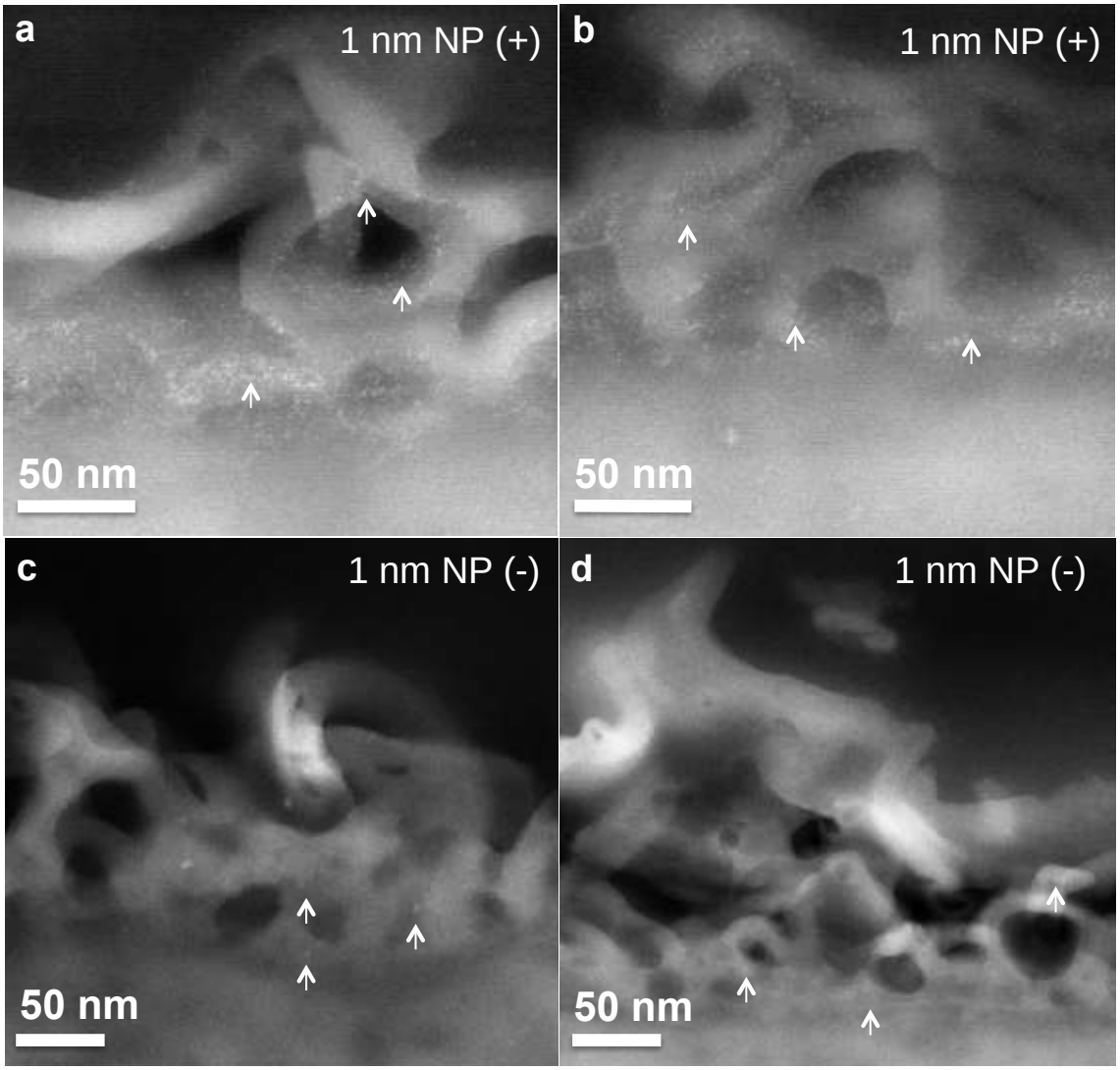

Figure 8 (a)-(b) STEM cross-sectional images of 1 nm (+) particles being back filtered into the membrane after 10 diavolume filtration and retarded by the polyamide film. (c)-(d) STEM cross-sectional images of 1 nm (-) particles which were back filtered into the membrane after 10 diavolume filtration and retarded by the polyamide film. There is observably more 1 nm (+) NP accumulation in the PA layer than 1 nm (-) NP, which corroborates with the results from dead-end filtration of NPs. The arrows indicate the location of nanoparticles.

4. Discussion

We have presented results which directly probe transport pathways in the PSf and PA layers of a representative RO membrane, for the first time. Nanometer sized pathways have been probed visually and confirmed using *in operando* filtration methods and a clear correlation between active transport across the membrane and

charge has been observed. Additionally, the roughness of the membrane and connectivity of void volumes have been investigated to elucidate how these may contribute to permeation.

The fractionation experiments carried out by back filtration of NPs of different sizes, analogous to size chromatography measurements, reveal a gradient of void dimensions available as transport pathways - from the μm sizes in PSf to nm sizes within the PA layer. NPs of 10 nm and above are retained within the PSf, while intermediate NPs (5 nm) reach the undulating folds at the PA-PSf interface, and only the 1 nm NPs are found to cross the PA-PSf interface, into the crumpled nodules on the top PA layer. The size barrier at the PA-PSf interface can thus be estimated to be around 1-5 nm. Further, whilst 1 nm particles of different charges can enter the PA layer, their distribution within the layer is shown to be charge-dependent, providing direct evidence that solute (e.g. ion) transport is governed by both size and charge. We note that, although the retention of 1 nm (+) and (-) NPs eventually approaches a similar value, its evolution over time (or diavolume) is clearly distinct, as shown in Figure 7. Such differences are interpreted as due to charge-mediated interactions with the membrane surface functional groups. (Additional front-filtration measurements and STEM images of 1 nm NP infiltration are provided in Supporting Information Figures S7 and S8, respectively).

This charge dependence is unsurprising given that the top and bottom surfaces of the PA layer are expected to have different charges. The top surface has reportedly a negative charge resulting from a concentration of 20-30 $–COO^-$ carboxylate functional groups per square nm.[2,34] The bottom surface is thought to be terminated

by positively charged amine groups ($-NH_3^+$) [34]. This asymmetry is compatible with our observations of positively charged particles lining the edge/outer surface of the membrane, presumably attracted to the negative charge of the carboxylate ions, and the negatively charged particles being predominantly found at the PSf-PA interface. Previous attempts have been made to investigate surface charge in PA membranes. Freger stained the top surface and bottom surfaces of RO membranes using sodium tungstate for the amino groups and uranyl acetate for carboxyl groups.[7] Given that (+) charged NPs accumulate preferentially on the PA front (and/or outer) surface, whereas (-) charged NPs exhibit a rather uniform distribution throughout the entire PA layer, our results are compatible with the expectation that PA films are negatively charged on the front side and positively charged on the back.[7] This appears to apply generally to MPD-TMC PA membranes and reconciles previously reported experimental facts concerning measurements of charge for this type of membrane.[2] Clearly more work can be done to understand the charge effects in permeation mechanisms and is currently underway.

Concerning the hollow inner nature of the PA wrinkles, recent studies by Yan *et al.* on a brackish water membrane[5] and Perera *et al.* [35] on an RO membrane have also found that the inner structure of the PA protuberances is hollow using SEM imaging of cryo-fractured, commercial and synthetic membranes. However, these studies do not probe the contribution of this morphology or surface area to flow permeability, nor resolve the dimensions of relevant permeation pathways across RO TFC membranes, made possible by our NP back-filtration experiments. Our TEM cross-sectional images reveal 1 nm (+) NPs residing within top protuberances of PA layer, as well as those isolated voids near the PA-PSf interface (Figure 9 and SI Figure S6). These hollow features therefore can be concluded to be flow active and likely impact the

hydrodynamic resistance and transport across RO membranes, contributing to the flow active area available for transport through the PA film.

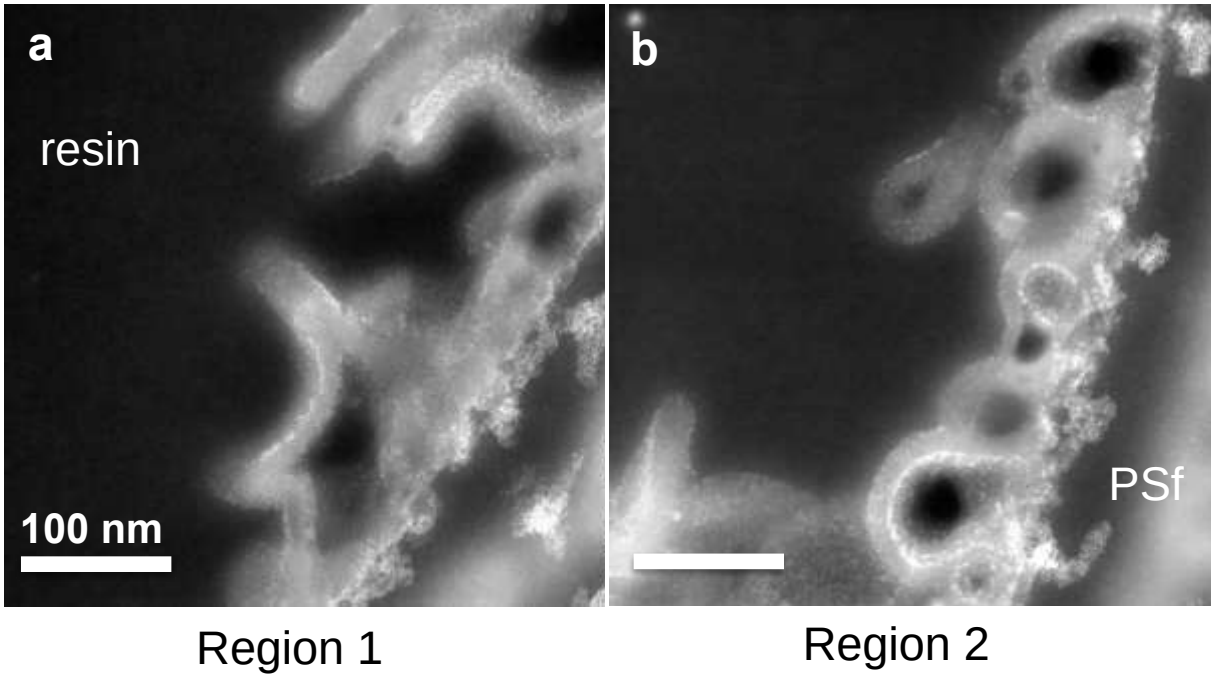

Figure 9: (a)-(b) STEM cross-sectional images of 1 nm (+) particles back-filtered into the membrane and lodged or retarded within the polyamide film, highlighting the flow active protruding nodular folds. Scale bars are 100 nm.

5. Conclusions

In this work, a combination of imaging techniques enabled a comprehensive study of the nanostructures of a model aromatic PA-based RO membrane. Our imaging results show that the crumpled features in the PA structures are internally hollow and flow active, and the PA-PSf interface is accessible to small NPs (1 nm), as shown by EM imaging. This finding agrees with previous report by Karan *et al* on the rigid crumpled nodules being able to withstand pressurized filtration, resulting in increased permeable area[6]. Based on the evidence of 1 nm NPs transport through the PA-PSf interface and reaching the interior of the crumpled nodules, we believe these flow-active features provide a higher actual permeable nanofilm area per unit area of the support membrane. Fractionation of back-filtered NPs across the RO layer and

selective distribution of negative and positively charged NPs demonstrate the potential of this approach as an *in-operando* probe into membrane nanostructure and function. The different charged 1 nm NPs labeled different regions of PA nanofilm corresponding to a distribution of functional groups at the PA front surface and the PA/PSf interface. This specific labeling of the 1 nm NPs reflects the sensitivity of the NP probing method in revealing chemical structures of polymeric membranes in addition to their physical structures.

Supporting Information

Supporting Information on additional membrane images (Figures S3-S5, S6, S9), nanoparticle characterization (Figure S1, Table S1) and filtration experimental results (Figures S2, S7) are available from the author.

Acknowledgements

We thank the BP International Centre for Advanced Materials (BP-ICAM) for funding and the Reverse Osmosis Memebrane Structure And Function (ROMSAF) team for stimulating discussions.

Received: ((will be filled in by the editorial staff))
Revised: ((will be filled in by the editorial staff))
Published online: ((will be filled in by the editorial staff))

References

[1] MaryTheresa M. Pendergast, and Eric M.V. Hoek. *Energy Environ. Sci.* **2011**, 4, 1946.

[2] Menachem Elimelech, and William A. Phillip. *Science **2011**,* 333, 712.

[3] Subhash C. Ayirala, Ernesto Uehara-Nagamine, Andreas Nicholas Matzakos, Robert W. Chin, Peter Harold Doe, Paul Jacob van den Hoek, *Society of Petroleum*

Engineers, **2010**, ISBN: 978-1-55563-289-2.

[4] Arnaud Lager, Kevin J. Webb, Cliff J. Black, Mike Singleton, Kenneth S. Sorbie, *Petrophysics* **2008**, 49, 28-35.

[5] Hao Yan, Xiaopei Miao, Jian Xu, Guoyuan Pan, Yang Zhang, Min Guo, Yiqun Liu, *J. Mem. Sci.* **2015**, 475, 504.

[6] Santanu Karan, Zhiwei Jiang, Andrew G. Livingston, *Science*, **2015**, 19, 1347.

[7] Viatcheslav Freger. *Langmuir* **2003**, 19, 4791.

[8] In-Chul Kim, Jonggeon Jegal, Kew-Ho Lee. *J. Poly. Sci. Part B: Poly. Phys.* **2002**, 40, 2151.

[9] Richard W. Baker, *Membrane Technology and Applications*, Wiley, 2nd Edition, West Sussex, UK, **2004**.

[10] Guy Z. Ramon, Eric M.V. Hoek, *J. Mem. Sci*. **2013**, 425, 141.

[11] Chuyang Y. Tang, Young-Nam Kwon, James O. Leckie. *J.Mem. Sci*. **2007**, 287, 146.

[12] Marvis C.Y. Wong, Lin Lin, Orlando Coronell, Eric M.V. Hoek, Guy Z. Ramon, *J. Mem. Sci*. **2016**, 500, 124.

[13] Lin Lin, Rene Lopez, Guy Z. Ramon, Orlando Coronell, *J. Mem. Sci*. **2016**, 497, 365.

[14] Federico Pacheco, Rachid Sougrat, Martin Reinhard, James O. Leckie, *J. Mem. Sci*. **2016**, 501, 33.

[15] Judy Lee, Anita Hill, Sandra Kentish, *Seperation and Purifation Tech*. **2013**, 104, 276.

[16] Federico A. Pacheco, Ingo Pinnau, Martin Reinhard, and James O. Leckie. *J. Mem. Sci.* **2010**, 358, 51.

[17] David G. Cahill, Viatches lav Freger, Seung-Yeop Kwak. *MRS Bull*. **2008**, 33, 27

[18] Baoxia Mi, Orlando Coronell, Benito J. Marinas, Fumiya Watanabe, David G. Cahill, Ivan Petrov. *J. Mem. Sci*. **2006**, 282, 71.

[19] Jan Kruse, Klaus Ratzke, Franz Faupel, Dana M. Sterescu, Dimitrios F. Stamatialis, Matthias Wessling, *J. Phys. Chem. B*. **2007**, 111, 13914

[20] Jonathan Albo, Hideaki Hagiwara, Hiroshi Yanagishita, Kenji Ito, Toshinori

Tsura. *Ind. Eng. Chem. Res*. **2014**, 53, 1442.

[21] Gerard Gebel, Jacques Lambard. *Macromolecules*. **1997**, 30, 7914.

[22] Wolfgang Pusch, Axel Walch. *J. Mem. Sci*. **1982**, 10, 325.

[23] Julia S. Higgins, Henry C. Benoit, *Polymers and Neutron Scattering*, Clarendon Press, Oxford, UK, **1994**.

[24] Massao Doi, Sam F. Edwards, *The Theory of Polymer Dynamics*, Clarendon Press, Oxford, UK,**1986**.

[25] Tania Rizwan, Subir Bhattacharjee, *The Canadian J. of Chem. Eng.* **2007**, 85, 570.

[26] Folkert Petrus Cuperus, Derk Bargeman, and Kees Smolders. *J. Colloid Interface Sci.* **1990,** 135, 486.

[27] Joanna Stawikowska, Maria F. Jimenez-Solomon, Yogesh Bhole, Andrew G. Livingston. *J. Membr. Sci.* **2013**, 442, 107.

[28] Joanna Stawikowska, Jeong F. Kim, Andrew G. Livingston. *J. Membr. Sci.* **2013**, 97, 81.

[29] Ludwig Reimer, *Energy-Filtered Transmission Electron Microscopy*. Springer Ser. Opt. Sci. 71, 373-375, **1994.**

[30] Avinash C. Kak, Malcolm Slaney, *Principles of Computerized Tomography Imaging*. IEEE, New York, US, **1998**.

[31] Michal M. Klosowski, Catriona M. McGilvery, Yuqiong Li, Joao T. Cabral, Andrew G. Livingston, Alexandra E. Porter, *J. Mem. Sci.* **2016**, 520, 465.

[32] Orlando Coronell, Benito J. Marinas, Xijing Zhang, David G. Cahill, *Environ. Sci. Technol*. **2008**, 42, 5260.

[33] Chuyang Y. Tang, Young-Nam Kwon, James O. Leckie, *Desalination*, **2009**, 242, 168.

[34] Viatcheslav Freger, *Environ. Sci. Technol*. **2004**, *38* (11), 3168–3175.

[35] Nimalika D.H. Perera, Qilei Song, Hazim Qiblawey and Easan Sivaniah, *J. Mem. Sci.* **2015**, 487, 74